This is a repository copy of *The cohesive band model: A cohesive surface formulation with stress triaxiality*.

White Rose Research Online URL for this paper:
http://eprints.whiterose.ac.uk/96206/

Version: Accepted Version

The Cohesive Band Model: A Cohesive Surface Formulation with Stress Triaxiality

Joris J.C. Remmers · **René de Borst** · **Clemens V. Verhoosel** · **Alan Needleman**

Abstract In the cohesive surface model cohesive tractions are transmitted across a two-dimensional surface, which is embedded in a three-dimensional continuum. The relevant kinematic quantities are the local crack opening displacement and the crack sliding displacement, but there is no kinematic quantity that represents the stretching of the fracture plane. As a consequence, in-plane stresses are absent, and fracture phenomena as splitting cracks in concrete and masonry, or crazing in polymers, which are governed by stress triaxiality, cannot be represented properly. In this paper we extend the cohesive surface model to include in-plane kinematic quantities. Since the full strain tensor is now available, a three-dimensional stress state can be computed in a straightforward manner. The cohesive band model is regarded as a subgrid scale fracture model, which has a small, yet finite thickness at the subgrid scale, but can be considered as having a zero thickness in the discretisation method that is used at the macroscopic scale. The standard cohesive surface formulation is obtained when the cohesive band width goes to zero. In principle, any discretisation method that can capture a discontinuity can be used, but partition-of-unity based finite element methods and isogeometric finite element analysis seem to have an advantage since they can naturally incorporate the continuum mechanics. When using interface finite elements, traction oscillations that can occur prior to the opening of a cohesive crack, persist for the cohesive band model. Example calculations show that Poisson contraction influences the results, since there is a coupling between the crack opening and the in-plane normal strain in the cohesive band. This coupling holds promise for capturing a variety of fracture phenomena, such as delamination buckling and splitting cracks, that are difficult, if not impossible, to describe within a conventional cohesive surface model.

Joris J.C. Remmers
Department of Mechanical Engineering
Eindhoven University of Technology
PO Box 513, 5600 MB, Eindhoven, The Netherlands E-mail: J.J.C.Remmers@tue.nl

René de Borst
University of Glasgow, School of Engineering,
Rankine Building, Oakfield Avenue, Glasgow G12 8LT, UK
E-mail: Rene.deBorst@glasgow.ac.uk

Clemens V. Verhoosel
Department of Mechanical Engineering
Eindhoven University of Technology
PO Box 513, 5600 MB, Eindhoven, The Netherlands E-mail: C.V.Verhoosel@tue.nl

Alan Needleman
Department of Materials Science and Engineering
College of Engineering and Center for Advanced Scientific Computing and Modeling,
University of North Texas,
Denton, TX 76203, USA
E-mail: needle@unt.edu

1 Introduction

Fracture lies at the heart of many failure phenomena of man-made and natural structures. Since the seminal work of Griffith [1] and Irwin [2] on brittle fracture a plethora of approaches to fracture have been developed, resulting in a rich literature. For quasi-brittle and ductile fracture, where the length of the fracture process zone is not small compared to a typical structural size, cohesive surface models, originally proposed by Dugdale[3] and Barenblatt [4], and later by Hillerborg and

co-workers [5] for concrete fracture, have proven particularly successful.

The cohesive surface model is very powerful, yet remarkable in its simplicity. It basically consists of a fracture initiation criterion, and after nucleation, crack opening is governed by the work of separation or fracture toughness. The fracture process zone is lumped into a single plane ahead of the crack tip. Its opening is governed by the shape of the decohesion curve, which sets the relation between the normal and the shear tractions across the crack surfaces on one hand, and the relative displacements between these surfaces on the other hand. Fracture is then a natural outcome of the loading process.

In spite of its conceptual simplicity the incorporation of cohesive surface models in simulation software such that cohesive crack propagation can be simulated in a predictive manner, free from the underlying discretisation, has proven a non-trivial task that has been a main issue in computational mechanics for the past thirty years. When the composition of the structure clearly indicates the potential fracture planes, as in lamellar materials, or when the fracture plane is known from experiments, a discrete formulation like the cohesive surface model can be incorporated in interface elements that *a priori* are inserted between continuum elements at predefined locations, e.g. [6–8]. This methodology has been generalised in [9], where interface elements were placed between *all* interelement boundaries, thus allowing for a greater flexibility in the cohesive crack path that can be obtained. Alternatively, a remeshing strategy has been proposed in [10]. More recently, the partition-of-unity property of finite element shape functions has been exploited to obtain a discretisation-independent path for cohesive cracks [11–15]. Furthermore, it has been shown that also isogeometric analysis provides an elegant and powerful tool to implement cohesive surface models without discretisation bias [16].

The necessity, at least in earlier days, to align discontinuities with existing mesh lines, or to use remeshing strategies for avoiding or ameliorating a mesh bias in computations of the propagation of a discontinuity, has prompted the search for methods in which the discontinuity was distributed, or smeared, over a finite domain. In finite element analyses, this was typically the tributary area assigned to an integration point. Bažant and Oh [17] have proposed the Crack Band Model, in which the cohesive surface model was cast into a continuum format, such that the zero-thickness interface in the original approach was replaced by a finite width w, in practice the size of the mentioned tributary area that belongs to an integration point. In this way, 'smeared-crack' analyses can be carried out for a fixed mesh. A

further development along this line is to refine the kinematics at the element level such that the crack band is properly represented at the element level. Starting from original ideas formulated in References [18,19] this approach has been further developed and has been cast into the framework of Enhanced Assumed Strain elements in [20].

The above 'smeared-crack' approaches can be cast within the framework of (anisotropic) continuum damage mechanics [21,22], and share the disadvantage of continuum damage models that they result in an ill-posed boundary value problem beyond a certain threshold level of loading because of loss of ellipticity. Well-posedness can be restored by nonlocal averaging schemes [23] or by adding spatial gradients to the material constitutive relation [24]. Continuum damage models are three-dimensional constitutive relations. This implies that the normal strain parallel to the crack band is directly available, and, via the constitutive relation, the normal stress in the crack band direction can be directly computed. Thus, failure modes in which stress triaxiality plays a role, i.e. when fracture depends on the hydrostatic stress level can be predicted in a natural manner using continuum damage approaches, see for instance successful computations for ductile failure of porous metals using the modified Gurson model [25,26].

In [27,28] a finite thickness band method was presented to model circumstances where a weak discontinuity precedes a loss of the stress carrying capacity as, for example, occurs in modelling ductile fracture using a rate independent constitutive relation. In that formulation, a finite thickness band is introduced when loss of ellipticity occurs at a material point (an integration point in a finite element implementation). The band thickness is regarded as a material parameter. Consistent with the kinematics of a weak discontinuity, see for example [29,30], the displacements vary linearly across the band. Also, the tractions are continuous across the band. The post-localisation material response in the band is governed by the pre-localisation constitutive relation together with the constraint imposed by the weak discontinuity kinematics, which can permit the tractions to vanish, creating new free surface, thus giving a transition from a weak to a strong discontinuity. In this formulation, the band thickness serves as a regularisation parameter.

A conventional zero thickness cohesive surface formulation involves a relation between tractions and displacement jumps across a surface. Stress components that do not affect the tractions are not accounted for in the cohesive constitutive relation and neither are deformation components that only involve displacements and gradients parallel to the surface. This limits the
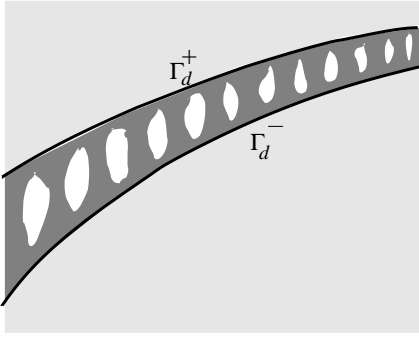
Fig. 1 A cohesive crack

Fig. 2 A cohesive band model

modeling capability in a variety of circumstances, including ductile failure of metals where stress triaxiality plays an important role and the prediction of splitting cracks in concrete or masonry structures where a large compressive stress creates cracks that are aligned with this normal stress [6]. One approach that has been proposed to overcome this limitation is to insert the normal stress from a neighbouring integration point in the continuum into the cohesive surface relation [31–33]. Another approach, as noted previously, is the finite band method of [27, 28].

Here, we introduce a cohesive surface thickness to directly model the evolution of fracture, which then straightforwardly allows for a dependence on all stress and deformation components. As a consequence, the approach here differs from that in [27, 28] in several significant aspects. First, the in-band response is taken to augment the cohesive surface relation so that, as in the usual cohesive surface formulation, the band constitutive relation is independent of the volumetric material relation. Indeed – and this is the second difference – the cohesive band model can be conceived as a sub-grid scale fracture model, with the band thickness a numerical parameter, rather than a material parameter, and the formulation is such that as the band thickness goes to zero, a conventional cohesive surface formulation is recovered. Finally, the present approach is fully discrete, with continuity of the discontinuity gap at element boundaries.

2 Band kinematics and virtual work

Attention is confined to small deformations and we consider the cohesive crack depicted in Figure 1. The thick lines are the cohesive surfaces Γ_d^- and Γ_d^+, characterised by the normals $\mathbf{n}_{\Gamma_d^-}$ and $\mathbf{n}_{\Gamma_d^+}$, respectively, see Figure 2. The thickness of the cohesive band Ω_b between the surfaces Γ_d^- and Γ_d^+ is denoted by h. The bulk $\Omega_B = \Omega \backslash \Omega_b$ consists of the sub-domain Ω^- that borders the cohe-

sive surface Γ_d^-, and the sub-domain Ω^+ that borders the cohesive surface Γ_d^+, Figure 2.
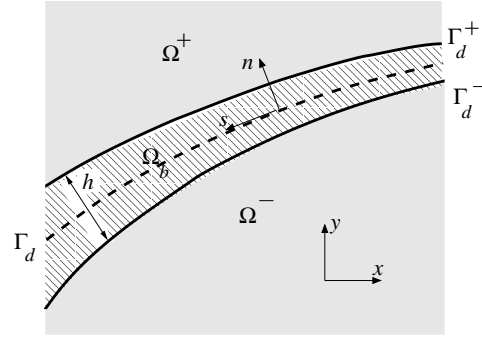
In the cohesive surface methodology a relation is assumed between the normal crack opening v_n and the crack sliding components v_s and v_t, assembled in a relative displacement vector $\bar{\mathbf{v}}$,

$$\bar{\mathbf{v}}^{\mathrm{T}} = (v_n, v_s, v_t)$$

and the normal traction t_n and the shear tractions t_s and t_t, assembled in the traction vector $\bar{\mathbf{t}}$, which is expressed in the n, s, t local reference frame:

$$\bar{\mathbf{t}}^{\mathrm{T}} = (t_n, t_s, t_t)$$

For consistency $\bar{\mathbf{v}}$ and $\bar{\mathbf{t}}$ must be decomposed in the same coordinate system.

The displacement $\mathbf{u}(\mathbf{x})$ of a material point in the body Ω can be expressed as:

$$\mathbf{u}(\mathbf{x}) = \hat{\mathbf{u}}(\mathbf{x}) + \mathcal{H}_{\Gamma_d} \tilde{\mathbf{u}}(\mathbf{x}) \tag{1}$$

with $\mathcal{H}_{\Gamma_d}$ the Heaviside function centered at the mid-surface of the cohesive band, Γ_d. Then, the displacement jump $\mathbf{v}$ equals the value of the additional displacement field at the discontinuity plane:

$$\mathbf{v}(\mathbf{x}) = \tilde{\mathbf{u}}(\mathbf{x}) \qquad \forall \ \mathbf{x} \in \Gamma_d \tag{2}$$

The displacement jump $\mathbf{v}$ is expressed in the global coordinate system. The transformation

$$\bar{\mathbf{v}} = \mathbf{T}\mathbf{v} \tag{3}$$

between the relative displacements in the current local coordinate system with the unit vectors $\bar{\mathbf{e}}_n$, $\bar{\mathbf{e}}_s$, $\bar{\mathbf{e}}_t$ and the displacement jump in the global coordinate system with unit vectors $\mathbf{e}_x$, $\mathbf{e}_y$, $\mathbf{e}_z$ is achieved using the transformation matrix $\mathbf{T}$, with components:

$$T_{ij} = \bar{\mathbf{e}}_i \cdot \mathbf{e}_j, \quad \text{where } \ i = [n, s, t], \ \ j = [x, y, z] \tag{4}$$

which is constructed using the unit vectors of the global coordinate system and those of the local coordinate system in the current configuration.

The strain tensor ϵ in the bulk $\Omega_B = \Omega \backslash \Omega_b$ is now derived in a standard manner:

$$\epsilon = \frac{1}{2}\left(\nabla \mathbf{u} + \nabla \mathbf{u}^{\mathrm{T}}\right) \qquad \forall \; \mathbf{x} \in \Omega_B \tag{5}$$

We further define the strain tensor in the cohesive band, expressed in the n, s, t local frame of reference of the band:

$$\bar{\boldsymbol{\mathcal{E}}} = \begin{bmatrix} \mathcal{E}_{nn} & \mathcal{E}_{ns} & \mathcal{E}_{nt} \\ \mathcal{E}_{sn} & \mathcal{E}_{ss} & \mathcal{E}_{st} \\ \mathcal{E}_{tn} & \mathcal{E}_{ts} & \mathcal{E}_{tt} \end{bmatrix} \qquad \forall \; \mathbf{x} \in \Omega_b \tag{6}$$

The components of this matrix are based on the magnitude of the relative displacements and on the in-plane strains in the band. The strain tensor $\bar{\boldsymbol{\mathcal{E}}}$ can be transformed to the local frame of reference using the transformation matrix $\mathbf{T}$:

$$\bar{\boldsymbol{\mathcal{E}}} = \mathbf{T}\boldsymbol{\mathcal{E}}\mathbf{T}^{\mathrm{T}} \tag{7}$$

with $\boldsymbol{\mathcal{E}}$ containing the components $\mathcal{E}_{xx}$ etc. in the global x, y, z coordinate system.

We now define a (small) band width h_0 as the value of the crack opening, h, in a reference state. Using the assumptions that the strains in the band are piecewise constant at either side of the discontinuity Γ_d in the n-direction, and that the normal strain component $\mathcal{E}_{nn}$, and the shear strain components $\mathcal{E}_{ns}$ and $\mathcal{E}_{nt}$ are completely determined by the crack opening v_n, and the crack sliding components v_s and v_t, respectively, we can define:

$$\mathcal{E}_{nn} = \frac{v_n}{h_0} \tag{8}$$

and

$$\mathcal{E}_{ns} = \frac{v_s}{2h_0} \tag{9}$$

$$\mathcal{E}_{nt} = \frac{v_t}{2h_0} \tag{10}$$

In a standard manner the virtual strain components can be derived as

$$\delta\mathcal{E}_{nn} = \frac{\delta v_n}{h_0} \tag{11}$$

and

$$\delta\mathcal{E}_{ns} = \frac{\delta v_s}{2h_0} \tag{12}$$

$$\delta\mathcal{E}_{nt} = \frac{\delta v_t}{2h_0} \tag{13}$$

The in-plane terms of the strain tensor in the band, $\mathcal{E}_{ss}, \mathcal{E}_{tt}$ and $\mathcal{E}_{st} = \mathcal{E}_{ts}$ are independent of the magnitude of the displacement jump. They represent the normal strain components in the s- and t-directions, respectively, and the in-plane shear strain. In view of the assumption that the strains in the band are piecewise

constant at either side of the discontinuity Γ_d in the n-direction, and enforcing continuity for the in-plane strain components across Γ_d^- and Γ_d^+ these strain components are defined as:

$$\mathcal{E}_{ss} = \frac{1}{2}\left(\mathcal{E}_{ss}|_{\Gamma_d^-} + \mathcal{E}_{ss}|_{\Gamma_d^+}\right)$$

$$\mathcal{E}_{tt} = \frac{1}{2}\left(\mathcal{E}_{tt}|_{\Gamma_d^-} + \mathcal{E}_{tt}|_{\Gamma_d^+}\right) \tag{14}$$

$$\mathcal{E}_{st} = \frac{1}{2}\left(\mathcal{E}_{st}|_{\Gamma_d^-} + \mathcal{E}_{st}|_{\Gamma_d^+}\right)$$

The internal virtual work of the solid can be expressed in terms of the stress tensor $\boldsymbol{\sigma}$ and the variation of the strain tensor. In the bulk of the domain, Ω_B, we denote the variation of the strain tensor by $\delta\epsilon$, while in the cohesive band, Ω_b, we have $\delta\boldsymbol{\mathcal{E}}$ denoting the variation of the strain tensor and $\boldsymbol{\mathcal{S}}$ the band stresses, so that:

$$\delta W_{\mathrm{int}} = \int_{\Omega_B} \boldsymbol{\sigma} : \delta\epsilon \, \mathrm{d}\Omega + \int_{\Omega_b} \boldsymbol{\mathcal{S}} : \delta\boldsymbol{\mathcal{E}} \, \mathrm{d}\Omega \tag{15}$$

This expression is formally identical to equation (30) of Reference [27], but, as alluded to in the Introduction, the interpretation of the second term is different. Herein, it strictly relates to the energy that is dissipated by the cohesive tractions and by the in-plane band stresses, and in the limiting case of a band with zero thickness, the energy expended by the cohesive tractions is retained. This is different from the approach in Reference [27,28], where the energy dissipation vanishes when the band width is zero.

The second term in equation (15), which represents the contribution of the cohesive band, can be rewritten as:

$$\delta W_{\mathrm{int}}\,|_{\Omega_b} = \int_{\Gamma_d} \int_{-\frac{h_0}{2}}^{\frac{h_0}{2}} \boldsymbol{\mathcal{S}} : \delta\boldsymbol{\mathcal{E}} \, \mathrm{d}n \mathrm{d}\Gamma \tag{16}$$

Again using the assumption that the deformation in the cohesive band is constant in the n-direction, we integrate analytically in the thickness direction:

$$\delta W_{\mathrm{int}}\,|_{\Omega_b} = h_0 \int_{\Gamma_d} \boldsymbol{\mathcal{S}} : \delta\boldsymbol{\mathcal{E}} \, \mathrm{d}\Gamma \tag{17}$$

or written in terms of the individual components:

$$\delta W_{\mathrm{int}}\,|_{\Omega_b} = h_0 \int_{\Gamma_d} (\mathcal{S}_{nn}\delta\mathcal{E}_{nn} + \mathcal{S}_{ss}\delta\mathcal{E}_{ss} + \mathcal{S}_{tt}\delta\mathcal{E}_{tt} + \\ 2\mathcal{S}_{ns}\delta\mathcal{E}_{ns} + 2\mathcal{S}_{nt}\delta\mathcal{E}_{nt} + 2\mathcal{S}_{st}\delta\mathcal{E}_{st}) \, \mathrm{d}\Gamma \tag{18}$$

which relation holds irrespective of the value of the cohesive band width h_0. Substitution of the expressions

for the virtual strains derived in equations (11), (12) and (14) gives:

$$\delta W_{\text{int}} |_{\Omega_b} = \int_{\Gamma_d} (\mathcal{S}_{nn}\delta v_n + h_0\mathcal{S}_{ss}\delta\mathcal{E}_{ss} + h_0\mathcal{S}_{tt}\delta\mathcal{E}_{tt} + \qquad (19)$$
$$\mathcal{S}_{ns}\delta v_s + \mathcal{S}_{nt}\delta v_t + 2h_0\mathcal{S}_{st}\delta\mathcal{E}_{st}) \, \mathrm{d}\Gamma$$

In the limit, i.e. when $h_0 \to 0$, this expression reduces to:

$$\delta W_{\text{int}} |_{\Omega_b} = \int_{\Gamma_d} (\mathcal{S}_{nn}\delta v_n + \mathcal{S}_{ns}\delta v_s + \mathcal{S}_{nt}\delta v_t) \, \mathrm{d}\Gamma \qquad (20)$$

or replacing the stress components $\mathcal{S}_{nn}$, $\mathcal{S}_{ns}$ and $\mathcal{S}_{nt}$ by the tractions t_n, t_s and t_s, we obtain the usual cohesive surface relation:

$$\delta W_{\text{int}} |_{\Omega_b} = \int_{\Gamma_d} (t_n\delta v_n + t_s\delta v_s + t_t\delta v_t) \, \mathrm{d}\Gamma \qquad (21)$$

The effect of the in-plane strains in the cohesive band, $\mathcal{E}_{ss}$, $\mathcal{E}_{tt}$ and $\mathcal{E}_{st}$, has now disappeared, as it should. We will come back to this in the example of Section 5.

To further elucidate how the tractions behave in the limit when the band width h_0 goes to zero, we consider the case that only the normal components across the band, $\mathcal{S}_{nn}$ and $\mathcal{E}_{nn}$ are non-zero. Then, equation (18) reduces to:

$$\delta W_{\text{int}} |_{\Omega_b} = h_0 \int_{\Gamma_d} \mathcal{S}_{nn}\delta\mathcal{E}_{nn}\mathrm{d}\Gamma \qquad (22)$$

From equation (8) we recall that

$$\mathcal{E}_{nn} = \frac{v_n}{h_0}$$

so that equation (22) can be rewritten as:

$$\delta W_{\text{int}} |_{\Omega_b} = \int_{\Gamma_d} S_{nn}\delta v_n\mathrm{d}\Gamma \qquad (23)$$

For simplicity, but without loss of generality, since any classical constitutive relation could have been used via integration of a rate relation, we suppose that the material in the band obeys a linear elastic constitutive relation with a Young's modulus in the band denoted by E_b:

$$\mathcal{S}_{nn} = E_b\mathcal{E}_{nn} = E_b\frac{v_n}{h_0} \qquad (24)$$

Equation (23) can now be written as:

$$\delta W_{\text{int}} |_{\Omega_b} = \int_{\Gamma_d} E_b\frac{v_n}{h_0}\delta v_n\mathrm{d}\Gamma \qquad (25)$$

We next take the limit $h_0 \to 0$. In this limit v_n also goes to zero, so it is a singular limit. However, equilibrium across the finite band cohesive surface requires continuity of tractions, so

$$E_b\frac{v_n}{h_0} = t_n$$

where t_n is the traction given by the constitutive relation outside the band. This must be satisfied for all h_0 and in particular in the limit $h_0 \to 0$. Hence,

$$\delta W_{\text{int}} |_{\Omega_b} = \int_{\Gamma_d} t_n\delta v_n\mathrm{d}\Gamma \qquad (26)$$

It is finally noted that a similar approach, in which a discontinuity has been modelled as a zero-thickness interface at the macroscopic scale, while a small, but finite thickness has been used for the modelling at a subgrid scale, has been used for modelling fluid flow in cracks or shear bands that are embedded in a surrounding porous medium [34–36].

3 Discretisation

As discussed in the Introduction, cohesive surface models can be discretised in a variety of ways, starting from interface elements, to partition-of-unity based finite element methods [11–15] and isogeometric analysis [16]. This holds also for the cohesive band model presented in the previous section, since the kinematic quantities known in this element in principle allow for the computation of the in-plane strains $\mathcal{E}_{ss}$, $\mathcal{E}_{tt}$ and $\mathcal{E}_{st}$. However, unlike interface elements, partition-of-unity based finite element methods naturally inherit the kinematics of the underlying continuum, also at the discontinuity Γ_d. For this reason we will adopt the partition-of-unity based finite element technology for embedding the cohesive band model developed in the preceding section. We note, however, that for the limiting case that the cohesive surface coincides with the edge of an element in a partition-of-unity approach, the structure of an interface element is recovered [37,38]. In particular, if the partition-of-unity approach is applied such that the discontinuity is defined *a priori* to coincide with the element edges, it inherits disadvantageous features such as traction oscillations which can occur prior to the opening of the discontinuity. In the next section we will investigate to which extent this also holds for the cohesive band approach.

For a set of shape functions ϕ_k that satisfy the partition-of-unity property, a field u can be interpolated as follows [39]:

$$u = \sum_{k=1}^{n} \phi_k \left(\hat{a}_k + \sum_{l=1}^{m} \psi_l\tilde{a}_{kl} \right) \qquad (27)$$

with $\hat{a}_k$ the 'regular' nodal degrees-of-freedom, ψ_l the enhanced basis terms, and $\tilde{a}_{kl}$ the additional degrees-of-freedom at node k, which represent the amplitudes of the lth enhanced basis term ψ_l. A basic requirement

of the enhanced basis terms ψ_l is that they are linearly-independent, mutually, but also with respect to the set of functions ϕ_k. In a conventional finite element notation we thus interpolate a displacement field as:

$$\mathbf{u} = \mathbf{\Phi}(\hat{\mathbf{a}} + \mathbf{\Psi}\tilde{\mathbf{a}}) \tag{28}$$

where $\mathbf{\Phi}$ contains the standard shape functions and $\mathbf{\Psi}$ the enhanced basis terms. The arrays $\hat{\mathbf{a}}$ and $\tilde{\mathbf{a}}$ collect the standard and the additional nodal degrees-of-freedom, respectively. A displacement field that contains a single discontinuity can be represented by taking [11–15, 40]:

$$\mathbf{\Psi} = \mathcal{H}_{\Gamma_d}\mathbf{I} \tag{29}$$

Substitution into equation (28) gives:

$$\mathbf{u} = \underbrace{\mathbf{\Phi}\hat{\mathbf{a}}}_{\hat{\mathbf{u}}} + \mathcal{H}_{\Gamma_d}\underbrace{\mathbf{\Phi}\tilde{\mathbf{a}}}_{\tilde{\mathbf{u}}} \tag{30}$$

Identifying the continuous fields $\hat{\mathbf{u}} = \mathbf{\Phi}\hat{\mathbf{a}}$ and $\tilde{\mathbf{u}} = \mathbf{\Phi}\tilde{\mathbf{a}}$ we observe that equation (30) exactly describes a displacement field that is crossed by a discontinuity Γ_d, but is otherwise continuous. Accordingly, the partition-of-unity property of finite element shape functions can be used in a straightforward fashion to incorporate discontinuities in a continuum such that their discontinuous character is preserved.

To derive the discretised set of equations we take the internal virtual work, equation (15), as point of departure, but we replace the second term by the expression of equation (17), which results after integration over the thickness of the band, and assume henceforth for simplicity of notation that the local and global coordinate systems coincide. Evidently, in the actual implementation one has to take care that the rotations are carried out properly. This results in:

$$\delta W_{\text{int}} = \int_{\Omega_B} \boldsymbol{\sigma} : \delta\boldsymbol{\epsilon}\,\mathrm{d}\Omega + h_0 \int_{\Gamma_d} \boldsymbol{\mathcal{S}} : \delta\boldsymbol{\mathcal{E}}\,\mathrm{d}\Gamma \tag{31}$$

In a Bubnov-Galerkin sense we assume that the test functions are taken from the same space as the trial functions modulo inhomogeneous boundary conditions, so that in view of equation (30):

$$\delta\mathbf{u} = \mathbf{\Phi}\delta\hat{\mathbf{a}} + \mathcal{H}_{\Gamma_d}\mathbf{\Phi}\delta\tilde{\mathbf{a}} \tag{32}$$

Substitution of equation (32) into equation (31) and requiring that the result holds for arbitrary $\delta\hat{\mathbf{a}}$ and $\delta\tilde{\mathbf{a}}$ yields the following set of coupled equations in matrix-vector notation:

$$\mathbf{f}_{\text{int}}^{\hat{\mathbf{a}}} = \int_{\Omega_B} \mathbf{B}^{\mathrm{T}}\boldsymbol{\sigma}\,\mathrm{d}\Omega + h_0 \int_{\Gamma_d} \hat{\mathbf{B}}^{\mathrm{T}}\boldsymbol{\mathcal{S}}\,\mathrm{d}\Gamma \tag{33a}$$

and

$$\mathbf{f}_{\text{int}}^{\tilde{\mathbf{a}}} = \int_{\Omega^+} \mathbf{B}^{\mathrm{T}}\mathbf{S}\,\mathrm{d}\Omega + \frac{1}{2}h_0 \int_{\Gamma_d} \tilde{\mathbf{B}}^{\mathrm{T}}\boldsymbol{\mathcal{S}}\,\mathrm{d}\Gamma \tag{33b}$$

where the Heaviside function has been eliminated from the volume integrals by a change of the integration domain from Ω_B to Ω^+. In the bulk, $\mathbf{B} = \mathbf{L}\mathbf{\Phi}$, the strain-nodal displacement matrix, with $\mathbf{L}$ an operator matrix, cf [22] – Chapter 2. Ordering the strains in the cohesive band as

$$\boldsymbol{\mathcal{E}}^{\mathrm{T}} = (\mathcal{E}_{nn}, \mathcal{E}_{ss}, \mathcal{E}_{tt}, \mathcal{E}_{ns}, \mathcal{E}_{nt}, \mathcal{E}_{st})$$

the matrices $\hat{\mathbf{B}}$ and $\tilde{\mathbf{B}}$ read:

$$\hat{\mathbf{B}} = \hat{\mathbf{L}}\mathbf{\Phi} \tag{34}$$

and

$$\tilde{\mathbf{B}} = \tilde{\mathbf{L}}\mathbf{\Phi} \tag{35}$$

with the operator matrices

$$\hat{\mathbf{L}} = \begin{bmatrix} 0 & 0 & 0 \\ 0 & \frac{\partial}{\partial s} & 0 \\ 0 & 0 & \frac{\partial}{\partial t} \\ 0 & 0 & 0 \\ 0 & 0 & 0 \\ 0 & \frac{\partial}{\partial t} & \frac{\partial}{\partial s} \end{bmatrix} \tag{36}$$

and

$$\tilde{\mathbf{L}} = \begin{bmatrix} \frac{1}{h_0} & 0 & 0 \\ 0 & \frac{1}{2}\frac{\partial}{\partial s} & 0 \\ 0 & 0 & \frac{1}{2}\frac{\partial}{\partial t} \\ 0 & \frac{1}{2h_0} & 0 \\ 0 & 0 & \frac{1}{2h_0} \\ 0 & \frac{1}{2}\frac{\partial}{\partial t} & \frac{1}{2}\frac{\partial}{\partial s} \end{bmatrix} \tag{37}$$

respectively.

Allowing for a wide range of cohesive relations, we postulate a tangential relation between the stress rate in the band

$$\dot{\boldsymbol{\mathcal{S}}}^{\mathrm{T}} = (\dot{\mathcal{S}}_{nn}, \dot{\mathcal{S}}_{ss}, \dot{\mathcal{S}}_{tt}, \dot{\mathcal{S}}_{ns}, \dot{\mathcal{S}}_{nt}, \dot{\mathcal{S}}_{st})$$

and the strain rate in the band, $\dot{\boldsymbol{\mathcal{E}}}$:

$$\dot{\boldsymbol{\mathcal{S}}} = \mathbf{D}_b\dot{\boldsymbol{\mathcal{E}}} \tag{38}$$

We assume that the tangential stiffness matrix $\mathbf{D}_b$ in the band has a transversely isotropic structure, and is obtained by differentiating the cohesive relation

$$\boldsymbol{\mathcal{S}} = \boldsymbol{\mathcal{S}}\left(\boldsymbol{\mathcal{E}}, \boldsymbol{\kappa}, E_b, \nu_b\right) \tag{39}$$

with $\boldsymbol{\kappa}$ an array of one or more internal variables, and E_b and ν_b the Young's modulus and the Poisson's ratio in the band, respectively. For the general three-dimensional case, a closed-form expression for $\mathbf{D}_b$ can

be rather complicated. For this reason, a compliance format is sometimes preferred:

$$\mathbf{D}_b^{-1} = \begin{bmatrix} \frac{1}{k_n} & -\frac{\nu_b}{E_b} & -\frac{\nu_b}{E_b} & 0 & 0 & 0 \\ -\frac{\nu_b}{E_b} & \frac{1}{E_b} & -\frac{\nu_b}{E_b} & 0 & 0 & 0 \\ -\frac{\nu_b}{E_b} & -\frac{\nu_b}{E_b} & \frac{1}{E_b} & 0 & 0 & 0 \\ 0 & 0 & 0 & \frac{1}{k_s} & 0 & 0 \\ 0 & 0 & 0 & 0 & \frac{1}{k_t} & 0 \\ 0 & 0 & 0 & 0 & 0 & \frac{2(1+\nu_b)}{E_b} \end{bmatrix} \tag{40}$$

with

$$k_n = \frac{\partial \mathcal{S}_{nn}}{\partial \mathcal{E}_{nn}}$$

the stiffness that derives from the cohesive relation for mode-I behaviour, and with

$$k_s = \frac{\partial \mathcal{S}_{ns}}{\partial \mathcal{E}_{ns}}$$

and

$$k_t = \frac{\partial \mathcal{S}_{nt}}{\partial \mathcal{E}_{nt}}$$

the tangential shear stiffnesses in the s- and t-directions, respectively. For plane-stress conditions, however, an explicit expression for the tangential stiffness matrix can easily be derived:

$$\mathbf{D}_b = \begin{bmatrix} \frac{E_b}{E_b k_n^{-1} - \nu_b^2} & \frac{\nu_b E_b}{E_b k_n^{-1} - \nu_b^2} & 0 \\ \frac{\nu_b E_b}{E_b k_n^{-1} - \nu_b^2} & \frac{E_b}{1 - \nu_b^2 E_b^{-1} k_n} & 0 \\ 0 & 0 & k_s \end{bmatrix} \tag{41}$$

We observe that the standard cohesive stiffnesses between the tractions and the relative displacements are incorporated, but that the matrix also includes the in-plane stiffness and the coupling between the normal relative displacement and the stretching of the fracture plane via the Poisson ratio ν_b in the band. The assumed transversely isotropic structure of equation (40) has limitations, in particular when ductile fracture processes are considered which involve metals, ductile polymers, or adhesives. An appropriate band constitutive relation could then involve a significant shear-normal stress/strain coupling and the response cannot be characterised by an isotropic constitutive relation.

4 Aspects of numerical integration

As stipulated in the preceding section the spatial numerical integration is an important issue in conventional interface elements when applied in the context of cohesive surface models, as they can suffer from spurious traction oscillations, in particular in quasi-brittle fracture where there is no compliant interface prior to
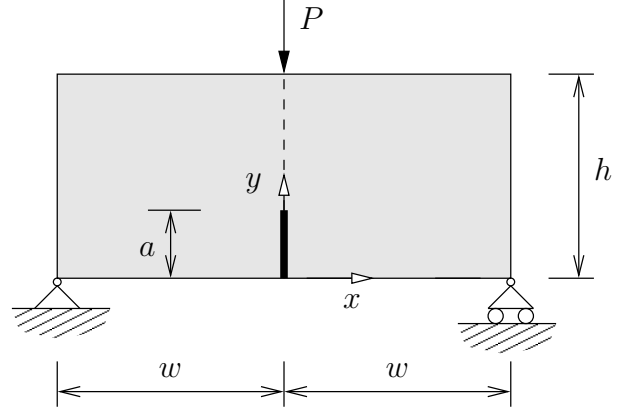

Fig. 3 Geometry and boundary conditions of a notched beam in a three-point bending test
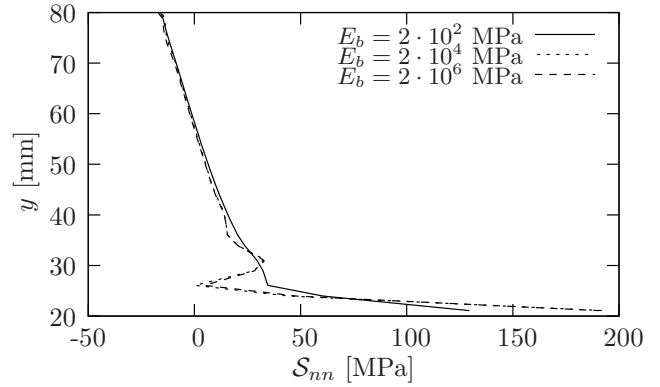

Fig. 4 Cohesive band stress $\mathcal{S}_{nn}$ as a function of the position at the interface for different magnitudes of the Young's modulus E_b in the cohesive band using a Gauss integration scheme
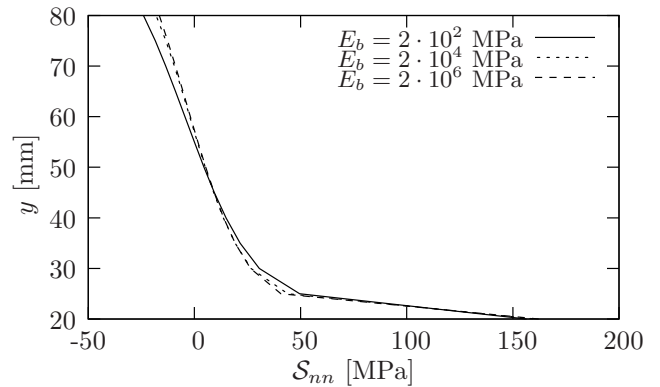

Fig. 5 Cohesive band stress $\mathcal{S}_{nn}$ as a function of the position at the interface for different magnitudes of the Young's modulus E_b in the cohesive band using a Newton-Cotes integration scheme
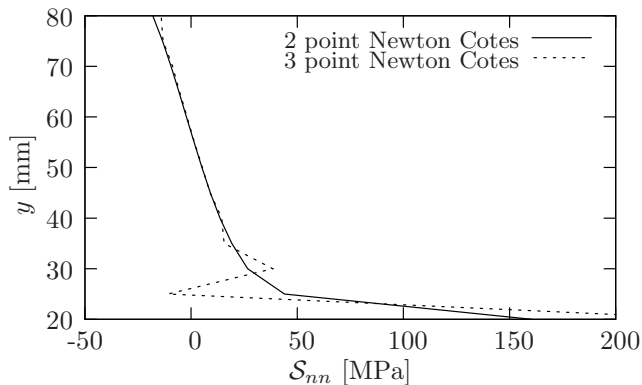
Fig. 6 Cohesive band stress $\mathcal{S}_{nn}$ as a function of the position at the interface for different Newton-Cotes integration schemes

Quadrilateral element   Triangular element

Fig. 7 Numerical integration of a quadrilateral and a triangular element. The triangulation of the sub-domains Ω^+ and Ω^- are denoted by the dashed lines; the corresponding integration points are denoted by the $\otimes$ symbols. The discontinuity Γ_d, represented by the bold line, is integrated by a two point Newton-Cotes scheme. These integration points are represented by the $\oplus$ symbols.

reaching the tensile strength. The magnitude of these oscillations increases with an increasing dummy stiffness, which is used prior to the opening of the discontinuity in order to ensure continuity [41]. A solution is to abandon Gauss integration and to resort to Newton-Cotes integration or to lumped integration techniques.

We will now investigate whether the interface elements equipped with a cohesive band model inherit this deficiency, which plagues interface elements that incorporate a cohesive surface model. For this purpose, we employ a notched three-point bending beam, shown in Figure 3, and used before in Reference [41]. The dimensions of the beam are $w = 125$ mm and $h = 100$ mm, and is made of an elastic, isotropic material with Young's modulus $E = 20\,000$ MPa and a Poisson's ratio $\nu = 0.2$. The length of the notch is $a = 20$ mm. The applied load is equal to $P = 1000$ N.

The finite element model consists of a structured grid of 51×20 four-noded bilinear elements. The interface is represented by a cohesive band. The notch, $0 < y < 20$ mm, is traction free, i.e. the tractions and the tangent stiffness matrix vanish, irrespective of the magnitude of the strain field. In the cohesive band, i.e. when $20 < y < 100$ mm, a linear-elastic, plane-strain constitutive relation is used. Calculations have been carried out for different magnitudes of the Young's modulus E_b in the cohesive band. The spatial integration along the cohesive band is done using either Gauss or Newton-Cotes integration. The traction profiles at the interface are shown in Figures 4 and 5.

The results for the cohesive band model confirm those obtained for a cohesive surface model [41] in the sense that traction oscillations are present when a Gauss integration scheme is used, and increase for larger values of the Young's modulus E_b in the band. Similarly, the traction oscillations disappear when a lumped integration scheme is used, Figure 5, but reappear when
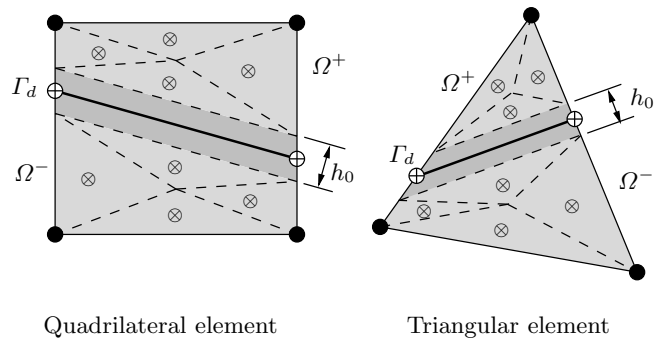
over-integration is used, Figure 6. In sum, standard interface elements show exactly the same behaviour with respect to spatial integration irrespective whether they are equipped with a cohesive surface model or with a cohesive band model.

The contributions of the bulk parts to the linear momentum equations of an element that is crossed by a cohesive band are integrated in a similar fashion as in Reference [11]. Both sub-domains Ω^+ and Ω^- are triangulated as shown in Figure 7. In the case of linear elements, each triangle is integrated by a single Gauss-point, denoted by the $\otimes$ sign. In order to ensure that the sum of the areas of the two bulk sub-domains and the cohesive band is equal to the area of the original undeformed element, the width of the cohesive band is taken into account during the triangulation of Ω^+ and Ω^-. Note that in the case of quadrilateral elements in combination with a structured mesh, the area of the cohesive band is equal to the length of the line Γ_d times the width h_0, see Figure 7. In the case of an unstructured mesh or triangular elements a small numerical error is introduced here. However, this error is negligible for small values of the band thickness h_0.

5 Double cantilever peel test

We next consider the double cantilever test shown in Figure 8. The structure with length $l = 10$ mm consists of two layers with the same thickness $h = 0.5$ mm and with the same (isotropic) material properties: a Young's modulus $E = 100$ MPa and a Poisson ratio $\nu = 0.3$. The two layers are connected through an adhesive with a tensile strength $t_{\max} = 1$ MPa and an interfacial fracture toughness $\mathcal{G}_c = 0.1$ N/mm. The initial delamina-
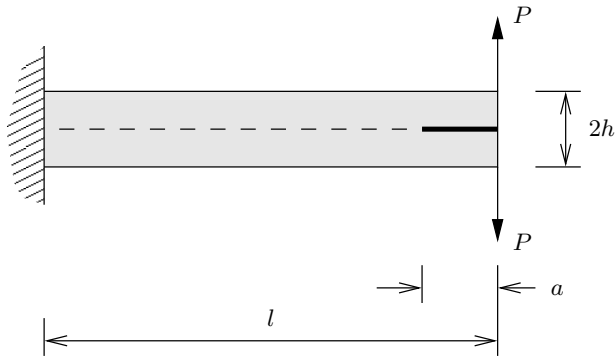
Fig. 8 Geometry and boundary conditions of a double cantilever peel test

Fig. 9 Effect of Poisson's ratio ν_b on the load-displacement curve for a cohesive band model

tion extends over $a = 1\,\text{mm}$. An external load P is applied at the tip of both layers.

The specimen has been analysed with four-noded quadrilateral elements: 100 elements in the horizontal direction and 11 elements in the vertical direction. The elements in the centre of the specimen, i.e. the elements that are crossed by the discontinuity, are square with dimensions $l_e \times l_e = 0.1 \times 0.1\,\text{mm}$. The solutions have been obtained using the energy dissipation arc-length method [42].

The constitutive behaviour of the cohesive band is governed by an isotropic, plane-strain continuum damage relation:

$$\boldsymbol{\mathcal{S}} = (1 - \omega)\mathbf{D}_b^e\boldsymbol{\mathcal{E}} \qquad (42)$$

where $\mathbf{D}_b^e$ is the plane-strain elastic stiffness matrix, that is constructed using the Young's modulus E_b and the Poisson's ratio ν_b in the band. The damage parameter ω is function of the history parameter κ, which is equal to the highest value of the principal strain locally obtained during the loading:

$$\omega = \begin{cases} 0 & \text{if } \kappa < \kappa_0 \\ \dfrac{\kappa_c}{\kappa}\dfrac{\kappa - \kappa_0}{\kappa_c - \kappa_0} & \text{if } \kappa_0 < \kappa < \kappa_c \\ 1 & \text{if } \kappa > \kappa_c \end{cases} \qquad (43)$$

In this relation, κ_0 and κ_c are defined as functions of the tensile strength $t_{\max}$ and a 'volumetric' fracture toughness g_c:

$$\kappa_0 = \frac{t_{\max}}{E_b}; \qquad \kappa_c = \frac{2g_c}{t_{\max}} \qquad (44)$$

The relation between the classical, interfacial fracture toughness $\mathcal{G}_c$ and the volumetric fracture toughness is:

$$g_c = \frac{\mathcal{G}_c}{h_0} \qquad (45)$$

The results of the simulations for different values of the Poisson's ratio in the band, ν_b, are compared
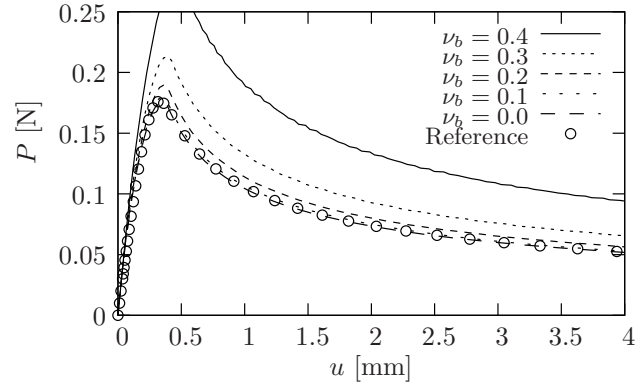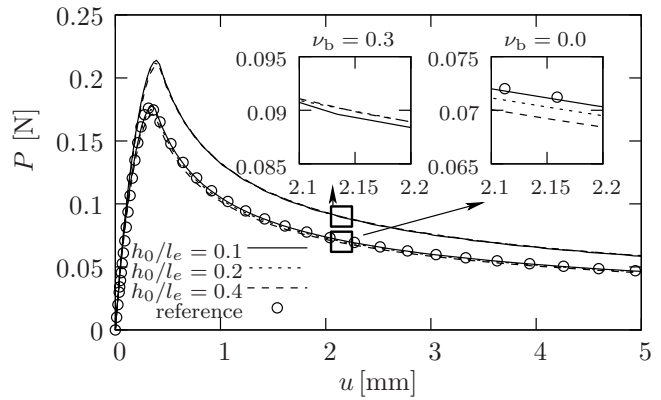

Fig. 10 Effect of the band thickness h_0 on the load-displacement curve for a cohesive band model. The effect is shown for two values of Poisson's ratio ν_b: 0.0 and 0.3.

with a standard cohesive surface model in Figure 9. We clearly observe the effect of the in-plane strains, which are generated through the coupling to the crack opening displacement through ν_b, the Poisson ratio in the band. The additional strains and ensuing stresses give rise to an additional term in the internal virtual work, thus resulting in a higher peak load and a more ductile behaviour. Evidently, the effect diminishes for smaller values of the Poisson's ratio, and disappears for $\nu_b = 0$, when the results of the standard cohesive surface model are retrieved.

Next, the effect of the band thickness h_0 is investigated. To this end, the simulations have been repeated for three different ratios $h_0/l_e = 0.1, 0.2$ and 0.4. The results are shown in Figure 10. Note that the mechanical behaviour is almost independent of the choice of cohesive band width h_0. For $\nu_b = 0.0$ the curve coincides with results for the standard cohesive surface model when h_0 is small. But even for non-zero values of Poisson ratio the results are almost independent of the band width.
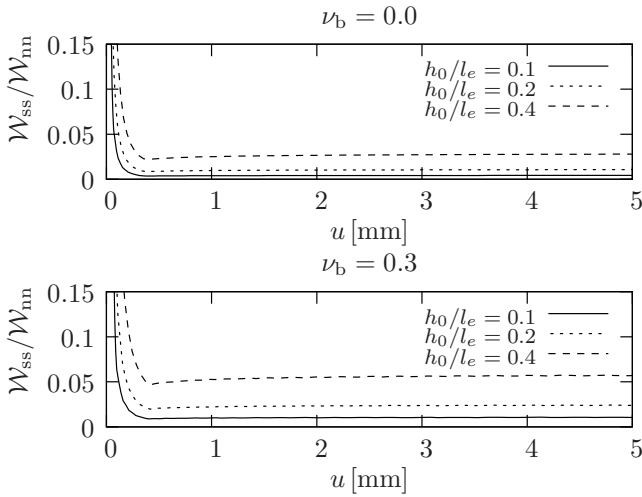
Fig. 11 The ratio of the stretch over the mode-I contributions to the elastic energy in the cohesive band as a function of the tip displacement u.

The contribution of the stretch term $\mathcal{E}_{\text{ss}}$ in the cohesive band becomes evident when we observe the contributions of all strain components to the internal energy. The ratio of the stretch over the normal (mode-I) contributions to the elastic energy is shown in Figure 11 as a function of the tip-displacement u. Evidently, the contribution of the relative magnitude of the stretch term to the elastic energy increases for an increasing ratio h_0/l_e, and is more pronounced for larger values of the Poisson ratio in the band, ν_b.

6 Concluding remarks

In this paper the cohesive band method has been presented as an extension of the cohesive surface model. At the macroscopic scale it resembles a standard cohesive surface model in the sense that fracture occurs over a discrete plane with zero thickness. Indeed, at this scale discretisation methods that are commonly used to incorporate cohesive surface formulations continue to be applicable. Also, anomalies that reside in certain discretisation methods, e.g. the traction oscillations that occur in conventional interface elements equipped with cohesive surface formulations and a high dummy stiffness to represent a non-compliant interface prior to reaching the tensile strength, persist, as has been shown for a classical example [41].

The cohesive band model deviates from standard cohesive surface formulations in the sense that a subgrid scale fracture model is conceived at the location of the discontinuity, which has a finite thickness, and which features a full three-dimensional strain and stress state. In the present implementation a transversely isotropic constitutive relation has been assumed within the band, which would focus on quasi-brittle fracture, rather than on ductile fracture, where shear-normal stress/strain couplings can become significant, and an anisotropic constitutive relation within the band may then be required. Along the same line, the isotropic continuum damage formalism that has been used in the example, is insufficient to model ductile fracture, where fracture is often preceded by plastic localisation. However, the constitutive relation for the band can be straightforwardly extended to incorporate anisotropy and plasticity. With appropriate constitutive relations the cohesive band formulation holds promise for capturing fracture phenomena such as splitting cracks in concrete and masonry under compressive axial stresses, crazing in polymers, and crack growth in porous metals, which all depend on stress triaxiality.

An important property of the cohesive band model is that it is consistent with standard cohesive surface formulations. Indeed, in the cohesive band model the strength and the ductility depend, in the constitutive formulation used here, on the Poisson ratio in the band, since the coupling between the crack opening displacement and the in-plane normal strains causes an additional term in the virtual work equation. However, we have shown that the cohesive band model reduces to the standard cohesive surface model for a vanishing band width. This is corroborated by numerical experiments, which show that the results from a standard cohesive surface model are obtained when the Poisson ratio in the band is set to zero, thus decoupling the in-plane normal strains from the crack opening displacement. The vanishing of the in-plane strains then implies that no longer additional work is expended, and the load-displacement curve becomes identical to that obtained for a standard cohesive surface model.

References

1. Griffith AA (1920) The phenomena of rupture and flow in solids, Philosophical Transactions **221**: 163–198.
2. Irwin GR (1957) Analysis of stresses and strains near the end of a crack traversing a plate, ASME Journal of Applied Mechanics **24**: 361–364.
3. Dugdale DS (1960) Yielding of steel sheets containing slits, Journal of the Mechanics and Physics of Solids **8**: 100–104.
4. Barenblatt GI (1962) The mathematical theory of equilibrium cracks in brittle fracture. Advances in Applied Mechanics **7**: 55–129.
5. Hillerborg A, Modeér M, Petersson PE (1976) Analysis of crack formation and crack growth in concrete by means of fracture mechanics and finite elements, Cement and Concrete Research **6**: 773–782.
6. Rots JG (1991) Smeared and discrete representations of localized fracture, International Journal of Fracture **51**: 45–59.

7. Schellekens JCJ, de Borst R (1993) A nonlinear finite-element approach for the analysis of mode I free edge delamination in composites, International Journal of Solids and Structures **30**: 1239–1253.

8. Needleman A (1987) A continuum model for void nucleation by inclusion of debonding, Journal of Applied Mechanics, **54**: 525–531.

9. Xu XP, Needleman A (1994) Numerical simulations of fast crack-growth in brittle solids, Journal of the Mechanics and Physics of Solids **42**: 1397–1434.

10. Camacho GT, Ortiz M (1996) Computational modelling of impact damage in brittle materials, International Journal of Solids and Structures **33**: 2899–2938.

11. Wells GN, Sluys LJ (2001) A new method for modelling cohesive cracks using finite elements. International Journal for Numerical Methods in Engineering **50**: 2667–2682.

12. Wells GN, de Borst R, Sluys LJ (2002) A consistent geometrically non-linear approach for delamination, International Journal for Numerical Methods in Engineering **54**: 1333–1355.

13. Moës N, Belytschko T (2002) Extended finite element method for cohesive cracks. Engineering Fracture Mechanics **69**: 813–833.

14. Remmers JJC, de Borst R, Needleman A (2003) A cohesive segments method for the simulation of crack growth, Computational Mechanics **31**: 69–77.

15. de Borst R, Remmers JJC, Needleman A (2006) Mesh-independent discrete numerical representations of cohesive-zone models, Engineering Fracture Mechanics **73**: 160–177.

16. Verhoosel CV, Scott MA, de Borst R and Hughes TJR (2011) An isogeometric approach to cohesive zone modeling, International Journal for Numerical Methods in Engineering **87**, 336-360.

17. Bažant ZP and Oh B. (1983) Crack band theory for fracture of concrete, RILEM Materials and Structures **16**: 155-177.

18. M. Ortiz and Y. Leroy and A. Needleman (1987) A finite element method for localized failure analysis, Computer Methods in Applied Mechanics and Engineering **61**: 189–214.

19. Belytschko T, Fish J, Engelman BE (1988) A finite element with embedded localization zones, Computer Methods in Applied Mechanics and Engineering **70**: 59–89.

20. Simo JC, Oliver J, Armero F (1993) An analysis of strong discontinuities induced by softening relations in rate-independent solids, Computational Mechanics **12**: 277–296.

21. de Borst R, Gutiérrez MA (1999) A unified framework for concrete damage and fracture models including size effects, International Journal of Fracture **95**: 261–277.

22. de Borst R, Crisfield MA, Remmers JJC, Verhoosel CV (2012) Non-linear Finite Element Analysis of Solids and Structures, Second Edition. Wiley, Chichester.

23. Pijaudier-Cabot G, Bažant ZP (1987) Nonlocal damage theory, ASCE Journal of Engineering Mechanics **113**: 1512–1533.

24. Peerlings RHJ, de Borst R, Brekelmans WAM and de Vree HPJ (1996) Gradient-enhanced damage for quasi-brittle materials, International Journal for Numerical Methods in Engineering **39**: 3391–3403.

25. Gurson AL (1977) Continuum theory of ductile rupture by void nucleation and growth. I. Yield criteria and flow rules for porous ductile media, ASME Journal of Engineering Materials and Technology **99**: 2–15.

26. Tvergaard V, Needleman A (1984) Analysis of the cup-cone fracture in a round tensile bar, Acta Metallurgica **32**: 157–169.

27. Huespe AE, Needleman A, Oliver J, Sanchez PJ (2009) A finite thickness band method for ductile fracture analysis, International Journal of Plasticity **25**: 2349-2365.

28. Huespe AE, Needleman A, Oliver J, Sanchez PJ (2012) A finite strain, finite band method for modeling ductile fracture International Journal of Plasticity **28**: 53-69.

29. Hill R (1962) Accelerations waves in solids, Journal of the Mechanics and Physics of Solids **10**: 1-16.

30. Rice JR (1976) The localization of plastic deformation. In: Theoretical and Applied Mechanics (Proceedings of the 14th International Congress on Theoretical and Applied Mechanics), Ed. Koiter WT, Volume 1, pp. 207-220. North-Holland, Amsterdam.

31. Keller K, Weihe S, Siegmund T, Kröplin B (1999) Generalized cohesive zone model: incorporating triaxiality dependent failure mechanisms, Computational Materials Science, **16**: 267-274

32. Tijssens MGA, van der Giessen E, Sluys LJ (2000) Modeling of crazing using a cohesive surface methodology, Mechanics of Materials **32**: 19–35.

33. Siegmund T, Brocks W (2000) A numerical study on the correlation between the work of separation and the dissipation rate in ductile fracture, Engineering Fracture Mechanics **67**: 139–154.

34. de Borst R, Réthoré J, Abellan MA (2006) numerical approach for arbitrary cracks in a fluid-saturated porous medium, Archive of Applied Mechanics **75**: 595–606.

35. Réthoré J, de Borst R, Abellan MA (2007) A discrete model for the dynamic propagation of shear bands in fluid-saturated medium, International Journal for Numerical and Analytical Methods in Geomechanics **31**: 347-370.

36. Réthoré J, de Borst R, Abellan MA (2008) A two-scale model for fluid flow in an unsaturated porous medium with cohesive cracks, Computational Mechanics **42**: 227-238.

37. Simone A (2004) Partition of unity-based discontinuous elements for interface phenomena: Computational issues, Communications in Numerical Methods in Engineering **20**: 465-478.

38. de Borst R (2006) Modern domain-based discretization methods for damage and fracture, International Journal of Fracture **138**: 241–262.

39. Babuska I, Melenk JM (1997) The partition of unity method, International Journal for Numerical Methods in Engineering **40**: 727-758.

40. Belytschko T, Black T (1999) Elastic crack growth in finite elements with minimal remeshing, International Journal for Numerical Methods in Engineering **45**: 601-620.

41. Schellekens JCJ, de Borst R (1993) On the numerical integration of interface elements, International Journal for Numerical Methods in Engineering **36**: 43–66.

42. Verhoosel CV, Remmers JJC, Gutiérrez MA (2009) A dissipation-based arc-length method for robust simulation of brittle and ductile failure, International Journal for Numerical Methods in Engineering **77**: 1290-1321.